internal powered plume flow downstream of the actuator disk. Under the conditions assumed, ϕ_1 and ϕ_2 satisfy the same $(1-M_\infty^2-M_\infty^2(\gamma+1)\phi_x)\phi_{xx}+\phi_{rr}+\phi_r/r=0$. For the external flow, $C_p=-2\phi_x$ is referenced to upstream conditions. For low-power levels, the internal C_p can also be referenced to the upstream dynamic head Q, so that $C_p=-2\phi_x+N$, NQ being the total pressure jump. Our approach assumes that power effects act primarily through slipstream boundary conditions rather than through changes in governing equation. This approach is simple because existing airfoil codes are modified easily. The matrix coefficients related to the differential equation need not be changed; in the difference algorithm used, the wake boundary condition $\phi_1(x,R)-\phi_2(x,R)=\phi_1(x_{te},R)-\phi_2(x_{te},R)-\frac{1}{2}N(x-x_{te})$ was applied on a mean radius R, x_{te} here referring to the trailing edge. This reduces to the usual relation for $N=0$. The nonlinear correction $N(1-M_\infty^2)(\phi_m(x_{te},R)-\phi_m(x_{te},R))/2$ to the right side, where $\phi_m=\frac{1}{2}(\phi_1+\phi_2)$, was also tested, and yielded no appreciable changes to results at transonic speeds. The derivatives ϕ_r and ϕ_{rr}, incidentally, were assumed to be continuous through the wake, so that explicit difference formulas are possible; this assumes small slipstream deflection angles consistently with small disturbance theory. The mean radius assumption, finally, is justifiable on one-dimensional grounds, because area (and, hence, radius) changes are only weakly dependent on changes in local Mach number; this and the use of fixed reference conditions in the differential equation place some restrictions on allowable pressure ratios.

III. Numerical Results and Closing Remarks

For simplicity, an external nacelle shape corresponding to a 10%-thick symmetric parabolic arc airfoil and an internal circular cylinder were used, with a chord-to-diameter ratio of 2. A coarse 60×60 constant mesh was taken, and two freestream Mach numbers, 0.92 and 0.98, were considered, in each case, assuming $N=0$ and a powered $N=3$ (large M_∞'s and N's were chosen to test numerical stability). Computed results should agree with this physical observation: engine power addition increases the mass flow passed by the nacelle, moving the inlet stagnation point from the inner toward the outer surface. Thus, the external shock present in the unpowered flow should disappear or reduce in strength in the powered case. This is seen from Figs. 1 and 2. The external shock present in the unpowered flows disappears completely with power addition; in both powered examples, the internal surface shows a localized and rapid inlet expansion peak terminated by a shock wave, indicating a stagnation point on the external surface that the fluid backs away from as it speeds supersonically into the engine face. This simple test problem, and several not reported here, show that the approach adopted here captures the basic feature of powered flows.

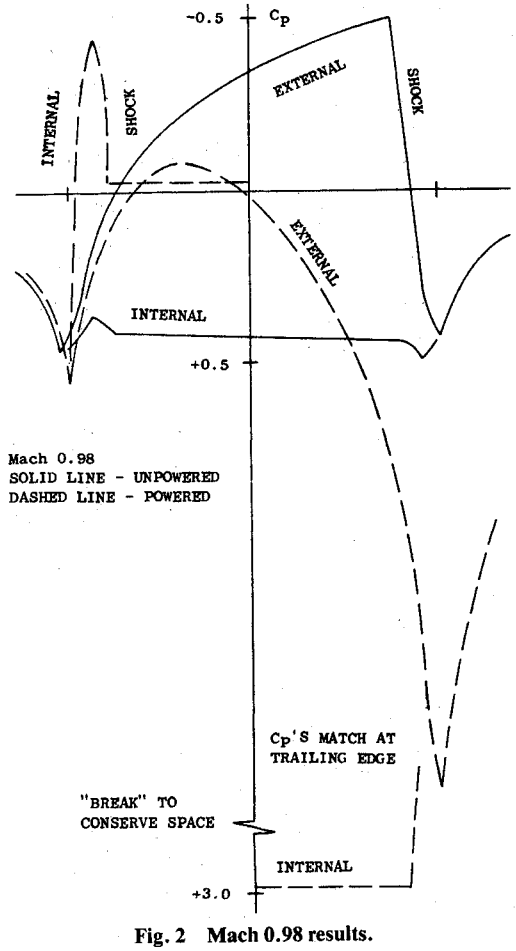

Fig. 2 Mach 0.98 results.

While we have considered here axisymmetric nacelles only, the basic ideas apply to three-dimensional flows as well, and may be useful in nacelle and wing interference studies. Again, as we have stressed throughout, our simplified approach applies only to small total pressure increases. Using different thermodynamic reference conditions would require the explicit use of actuator disk Fortran logic, plus additional matching conditions needed for the assumed disk model. Our column relaxation procedure, which "sweeps" through the disk from upstream to downstream without stopping, implicitly yields smooth and continuous ϕ_x's and ϕ_r's, the required pressure discontinuities appearing only when the converged $\phi(x,r)$ field is postprocessed using the respective C_p formulas. It is hoped that these early encouraging results will stimulate further research along these lines.

References

[1] Reyhner, T. A., "Transonic Potential Flow Computation About Three-Dimensional Inlets, Ducts, and Bodies," *AIAA Journal*, Vol. 19, Sept. 1981, pp. 1112-1121.

[2] Knight, D., "Numerical Simulation of Realistic High Speed Inlets Using the Navier-Stokes Equations," *AIAA Journal*, Vol. 15, Nov. 1977, pp. 1583-1589.

[3] Chaussee, D. S. and Pulliam, T. H., "Two-Dimensional Inlet Simulation Using a Diagonal Implicit Algorithm," *AIAA Journal*, Vol. 19, Feb. 1981, pp. 153-159.

[4] Kumar, A., "Two-Dimensional Analysis of a Scramjet Inlet Flowfield," *AIAA Journal*, Vol. 20, Jan. 1982, pp. 96-97.

[5] Chin, W. C., "Superpotential Solution for Jet Engine External Potential and Internal Rotational Flow Interaction," *ASME Journal of Applied Mechanics*, Vol. 50, June 1983, pp. 259-264.

[6] Golden, D. P., Barber, T. J., and Chin, W. C., "An Axisymmetric Nacelle and Turboprop Inlet Analysis with Flow-Through and Power Simulation Capabilities," AIAA Paper 82-0256, Orlando, Fla., Jan. 1982; *Journal of Aircraft*, Vol. 20, June 1983, pp. 536- 542.

Vibration of Triangular Plates

Shaukat Mirza* and Mohan Bijlani†
University of Ottawa, Ottawa, Canada

Nomenclature

a,b,h	= fixed length, cantilever length, and thickness of plate
$\|D\|$	= flexural rigidity matrix
D	= flexural rigidity, $Eh^3/\|12(1-\nu^2)\|$

Received Aug. 23, 1982; revision received Nov. 19, 1982.

*Professor, Department of Mechanical Engineering.
†Research Assistant, Department of Mechanical Engineering.

$N_i(\xi,\eta)$ = shape functions
$T^{(e)}, U^{(e)}$ = kinetic or potential energy of an element
w = transverse deflection of plate
x,y = Cartesian coordinates
η,ξ = nondimensional coordinates
κ = curvature parameter
ν,ρ = Poisson's ratio and the mass density of the plate
ϕ = aspect ratio, b/a
ω = circular frequency, rad/s

Introduction

TRANSVERSE vibration of homogeneous plates has been a subject of study for a long time. The problems of vibration of rectangular and circular plates have been extensively investigated by many researchers and are well documented. On the contrary, the work on triangular and other polygonal plates is rather limited. Earlier work on the triangular plates was restricted to delta (right angle) plates,[1,2] isosceles, and equilateral plates.[3-5] Gustafson and Stokey attempted a more general problem of swept-back plates using experimental techniques.[6] Subsequently, several other attempts were made[7] on the dynamics of plates of nonlinear materials.

In this Note, an attempt is made to present the effect of sweepback angle on the vibration of triangular plates. A finite element technique is used. The triangular plate-bending element used here has nine degrees of freedom and was developed earlier by Bazeley et al.[8] While generating the data, the authors felt that it would be convenient if the mathematical expressions for various quantities associated with this element were stated in terms of nondimensional quantities. A brief description of the proposed nondimensionalization is given in the next section. Consistent stiffness and mass matrices have been generated using a numerical integration technique. The solution for the nondimensional frequency parameter and modal shapes are presented graphically.

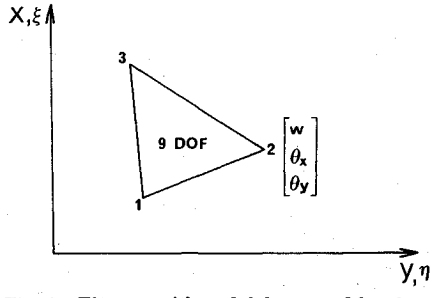

Fig. 1 Element with nodal degrees of freedom.

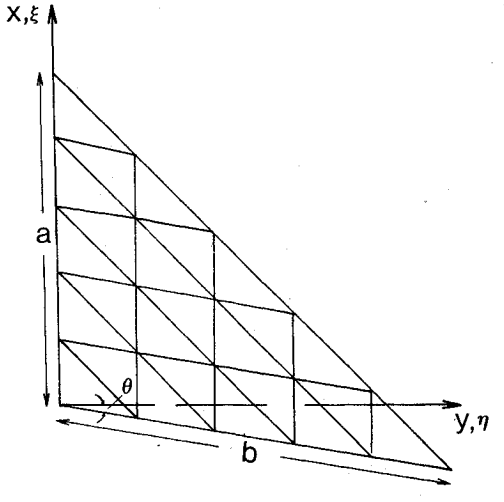

Fig. 2 Plate geometry and mesh pattern.

Solution Procedure

Figure 1 shows a typical triangular element with the nine degrees of freedom w_i, θ_{xi}, and θ_{yi}, where θ_x and θ_y represent the rotations about the x and y axes given by $-\partial w/\partial y$ and $\partial w/\partial x$, respectively. The element chosen here is nonconforming. The displacement function $w(x,y)$ in its general form is written as

$$w(x,y) = [N(x,y)]\{w\}^{ne} \tag{1}$$

Figure 2 shows the plate geometry with the orthogonal Cartesian (x,y) axes as well as the nondimensional (ξ,η) axes. Introducing the area coordinates L_i, $i=1,2,3$ in Eq. (1) and nondimensionalizing, we get

$$\hat{w} = w/a = \sum_{i=1}^{3} \left[{}_1N_i \quad \frac{{}_2N_i}{b} \quad \frac{{}_3N_i}{a} \right] \begin{Bmatrix} \hat{w}_i \\ -\partial\hat{w}/\partial_\eta\,|_i \\ \partial w/\partial\xi\,|_i \end{Bmatrix} \tag{2}$$

The shape functions ${}_1N_i$, ${}_2N_i$, ${}_3N_i$ for this element are

$$N_I^T = \begin{Bmatrix} {}_1N_I \\ {}_2N_I \\ {}_3N_I \end{Bmatrix}$$

$$= \begin{vmatrix} L_I^2 + L_I^2L_2 + L_I^2L_3 - L_IL_2^2 - L_IL_3^2 \\ b_3(L_I^2L_2 + \tfrac{1}{2}L_IL_2L_3) - b_2(L_3L_I^2 + \tfrac{1}{2}L_IL_2L_3) \\ c_3(L_I^2L_2 + \tfrac{1}{2}L_IL_2L_3) - c_2(L_3L_I^2 + \tfrac{1}{2}L_IL_2L_3) \end{vmatrix} \tag{3}$$

In the above matrices, the coefficients b and c are given by

$$b_2 = y_3 - y_I, \qquad b_3 = y_I - y_2$$
$$c_2 = x_I - x_3, \qquad c_3 = x_2 - x_I \text{ etc.} \tag{4}$$

b_i and c_i above can be easily nondimensionalized by dividing the above parameters by b and a in that order, which yields

Table 1 Values of the nondimensional frequency parameter Ω for three aspect ratios

Ω	θ, deg 0	15	30	45
		Aspect ratio = 1		
1	0.9802	0.9213	0.9178	0.9501
2	3.6703	3.3615	3.3583	3.6559
3	5.2981	5.4044	5.7216	6.5044
4	8.8992	8.2802	8.6171	10.0178
5	11.8550	10.9585	10.7308	11.6129
6	15.8305	15.8990	16.3227	18.1693
		Aspect ratio = 1.5		
1	0.5645	0.6315	0.5277	0.5453
2	2.3880	2.1833	2.1377	2.2311
3	3.5985	3.6639	3.8834	4.4109
4	6.1263	5.7313	5.8399	6.3905
5	8.5470	7.9539	7.9899	9.1103
6	12.5137	11.8966	11.6459	12.1558
		Aspect ratio = 2		
1	0.3768	0.3577	0.3545	0.3681
2	1.6599	1.5449	1.5159	1.5651
3	2.8704	2.8924	3.0675	3.4527
4	4.3755	4.1951	4.3093	4.7617
5	6.9082	6.4392	6.5828	7.7187
6	9.4412	9.2887	9.2550	9.5294

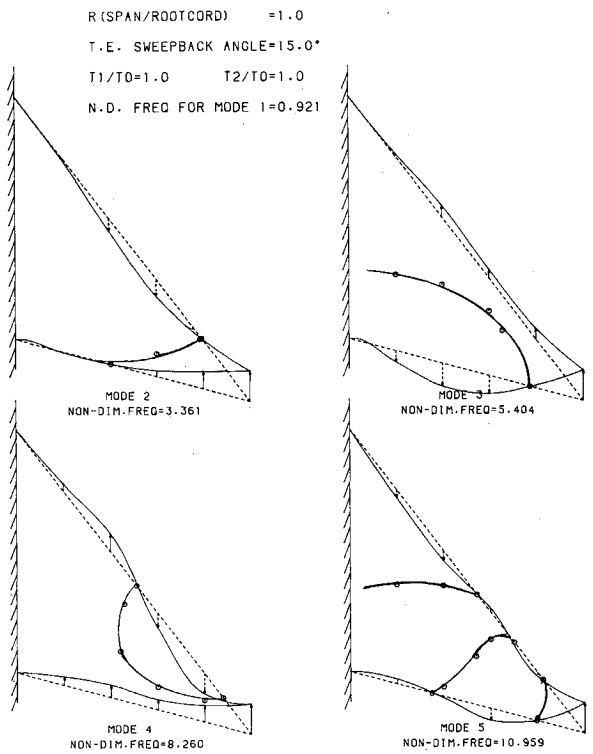

Fig. 3 Triangular plate mode shapes.

Table 2 Frequency parameter Ω′ (cycles) for right triangular plates

Mode	Experimental values, Ref. 6	High precision element, Ref. 9	Triangular element, present authors
1	0.9238	0.9801	0.9803
2	3.6418	3.7302	3.6703
3	5.0878	5.1976	5.2981
4	8.7028	8.9385	8.8992
5	11.8091	12.1947	11.8550
6	15.4777	15.8847	15.8306

the following:

$$b_3/b=\eta_1-\eta_2, \qquad c_3/a=\xi_2-\xi_1 \text{ etc.}$$

This will facilitate the nondimensionalization of the shape functions. With this assumption, the strain energy is written as

$$U^{(e)}=\frac{1}{2}\{\hat{w}\}^{ne^T}\left[\phi\int\int_{\Delta^*}[\hat{\kappa}_N]^T[D][\hat{\kappa}_N]\mathrm{d}\xi\mathrm{d}\eta\right]\{\hat{w}\}^{ne} \quad (5)$$

In Eq. (5), the quantity within the brackets, i.e.,

$$\phi\int\int[\hat{\kappa}_N][D][\hat{\kappa}_N]\mathrm{d}\xi\mathrm{d}\eta$$

is defined as the elemental stiffness, where the modified nondimensional curvature parameter $\hat{\kappa}_N$ is defined as

$$\{\hat{\kappa}_N\}=\left\{-\frac{\partial^2\hat{N}}{\partial\xi^2} \quad -\frac{\partial^2\hat{N}}{\partial\eta^2} \quad \frac{2\partial^2\hat{N}}{\partial\xi\partial\eta}\right\}$$

The element kinetic energy can be expressed in a simplified form:

$$T=\frac{1}{2}\rho\omega^2 ha^3 b\{\hat{w}\}^{ne^T}\left[\int\int_{\Delta}\hat{N}^T\hat{N}\mathrm{d}\xi\mathrm{d}\eta\right]\{\hat{w}\}^{ne} \quad (6)$$

Table 3 Frequency parameter Ω′ (cycles) for simple-supported equilateral plates

Mode	Ref. 5	Present authors
$n=m=1$	8.380	8.296
$n=1, m=2$	19.531	19.982
$n=2, m=1$	19.531	20.343
$n=2, m=2$	33.32	32.326

In Eqs. (5) and (6), the symbol (ˆ) denotes nondimensionality.

Computation and Results

The computation is effectively carried out by varying two geometric parameters, namely, the aspect ratio and the sweepback angle θ as shown in Fig. 2. Calculations have been performed by setting Poisson's ratio $\nu=0.3$. It is convenient to introduce a nondimensional frequency parameter Ω, which is defined as

$$\Omega=\omega\sqrt{\rho a^4\phi h/D} \quad (7)$$

In order to achieve proper convergence, several sets of calculations are performed in which the number of elements is varied. In this problem, good convergence is attained with 25 elements. A typical mesh is shown in Fig. 2. The stiffness and mass matrices are generated by using a three-point numerical integration scheme. Table 1 shows values of the nondimensional frequency parameter Ω for three aspect ratios, $\phi=1$, 1.5, 2.0, and $\theta=0$, 15, 30, 45 deg. As defined earlier, ω is in rad/s, consequently Ω, as introduced in Eq. (7), is also in radian units. However, for the purpose of comparison, the values of Ω in Tables 1 and 2 are presented in cycle units.

Results for some delta triangular plates are available in the literature.[6,9] Some of the results obtained here for the case $\theta=0$ plate can be compared with those in Refs. 6 and 9.

Table 2 gives the frequency parameter, converted to cycle units, for the right triangular plates. Comparison has been made with the experimental results found in Ref. 6 and with the results obtained by using a high precision finite element.[9] Comparing the present values with those in Ref. 6 for right triangular plates shows a maximum discrepancy of 5.7%, which occurs at the first mode. The rest of the frequencies show even better agreement, which is within 3%. It can be seen that, using the present simple and effective element, the results are excellent, and the agreement between the last two columns of Table 2 is very close. The maximum variation in this case is 2.8%, which occurs for the frequency value of the fifth mode. Table 3 shows the comparison of results for equilateral triangular plates. The same element and the solution routine discussed herein have been used to develop results for equilateral triangular plates with all of its three sides considered simple-supported. These values have been compared with the analytical values generated by Williams et al.,[5] which are shown in column 2 of Table 3. As can be seen, the results compare very well, and the maximum deviation, which is 3.9%, occurs for the third frequency.

Figure 3 shows some typical mode shapes. The broken lines in these figures show the undeformed plate. The solid lines show the deformed configuration of the plate for specific modes. The nodal lines are identified by small circles connected by a thick solid line. The nodal line for the fundamental mode, which is not shown, will exist along the supported edge.

References

[1] Christensen, R. M., "Vibration of a 45° Right Triangular Cantilever Plate by a Gridwork Method," *AIAA Journal*, Vol. 1, Aug. 1963, pp. 1790-1795.

[2] Hanson, P. W. and Tuovila, W., "Experimentally Determined Natural Vibration Modes of Some Cantilever Wing Flutter Models by Using an Acceleration Method," NACA TN 4010, 1957.

[3]Kumaraswamy, M. P. and Cadambe, V., "Experimental Study of the Vibration of Cantilevered Isoscels Triangular Plates," *Journal of Scientific and Industrial Research* (India), Vol. 15B, No. 2, 1956, pp. 54-60.

[4]Ota, T., Hamada, M., and Tarumoto, T., "Fundamental Frequency of an Isosceles Triangular Plate," *Bulletin of the Japan Society of Mechanical Engineers*, Vol. 4, No. 15, 1961, pp. 478-481.

[5]Williams, R., Yeow, Y. T., and Branson, H. F., "An Analytical and Experimental Study of Vibrating Equilateral Triangular Plates," *SESA Spring Meeting Proceedings*, Chicago, May 1975.

[6]Gustafson, P. N., Stokey, W. F., and Zorowski, C. F., "An Experimental Study of Natural Vibrations of Cantilevered Triangular Plates," *Journal of the Aerospace Sciences*, Vol. 20, 1953, pp. 331-337.

[7]Hewitt, J. S. and Mazumdar, J., "Vibration of Viscoelastic Triangular Plates," *Journal of Engineering Mechanics Division*, ASCE, Vol. 100, No. 6, Dec. 1974, pp. 1143-1146.

[8]Bazeley, G. P., Cheung, Y. K., Irons, B. M., and Zienkiewicz, O. C., "Triangular Elements in Plate Bending-Conforming and Non-Conforming Solutions," *Proceedings of the Conference on Matrix Methods in Structural Mechanics*, WPAFB, Ohio, Oct. 1965, pp. 547-576.

[9]Cowper, G. R., Kosko, E., Lindberg, G. M., and Olson, M. D., "Static and Dynamic Application of High Precision Triangular Plate Bending Elements," *AIAA Journal*, Vol. 7, Oct. 1969, pp. 1957-1965.

Integrated Thermal-Structural Approach for Shells of Revolution

Dennis J. Fallon* and Earl A. Thornton†
Old Dominion University, Norfolk, Virginia

Introduction

THE behavior of shells in severe thermal environments is important in current research on aerospace vehicles. The complex flowfields over missiles and other re-entry vehicles subject their shells to severe aerodynamic heating which requires detailed thermal and structural analyses. Practical shell structures are often analyzed by coupling a finite difference thermal analysis with a finite element structural analysis. Because of basic differences between analytical models an efficient interface is difficult to achieve, and extensive data processing may be required between thermal and structural analyses. The purpose of this Note is to present an integrated thermal-structural analysis for two dimensional shells of revolution. The integrated thermal-structural analysis approach will be considered for thermal prestress effects on aerodynamic instability of shells.

Integrated Finite Element Approach

To more fully develop the potential of the finite element method for thermal-stress analysis the concept of integrated thermal-structural analysis was proposed in Ref. 1. The objectives of the approach are to provide more efficient coupling of the thermal and structural analyses and improve the accuracy of the thermal-stress analysis. The approach is characterized by a common discretization for the thermal and structural analyses utilizing improved thermal elements to predict more detailed temperature variations, and equivalent thermal loads computed with temperature distributions from the improved thermal elements. The key to the approach is the development of new thermal elements which predict more detailed element temperature distributions while maintaining a common discretization with standard structural elements.

The approach used in this Note is to couple a steady-state, one-dimensional thermal finite element analysis with thickness-averaged temperature to a two-dimensional membrane-bending analysis of a shell of revolution. Since shell temperatures are predicted exactly, the thermal prestress effects on the structural response will be considered without loss of accuracy in the structural analysis. The first step in the solution is a thermal analysis whose results can either be nodal temperatures, as in the conventional finite element approach, or a temperature function, as in the integrated finite element approach. In the integrated approach, the results of the thermal analysis are incorporated consistently in a linear structural analysis to obtain thermal prestressing in both the circumferential and meridional direction. Herein lies the difference between the integrated finite element approach and the conventional finite element approach. In the conventional finite element approach the structural analyst is furnished only nodal temperatures from the thermal analysis; hence, the analyst assumes a function (usually linear) to describe the temperature between nodes to perform the necessary integration. However, in integrated finite element analysis there is no need to make this approximation since the actual temperature distribution is furnished from the thermal analysis.

The membrane stress then can be incorporated via the initial (or geometric) stress matrix to evaluate its effects on aerodynamic instability (flutter). This is expressed by the following eigenvalue problem:

$$|[K_e]+[K_g]+\lambda[A_e]-\omega^2[M]|=0 \tag{1}$$

where $[K_e]$ is the linear stiffness matrix, $[K_g]$ the initial stress matrix, $[A_e]$ the aerodynamic matrix, $[M]$ the mass matrix, λ the aerodynamic coefficient, and ω the natural frequency.

Finite Element Modeling

The exact thermal finite element formulation is based on conservation of energy for a shell of revolution. For axisymmetric conditions the energy equation has the general form[2]

$$\frac{d}{ds}\left[P(s)\frac{dT}{ds}\right]+Q(s)T=R(s) \tag{2}$$

where the temperature T is a function of the meridional coordinate s. Equation (2) may combine conduction with convection, internal heat generation, or surface heating.

Exact interpolation functions for the finite element formulation of Eq. (2) can be derived from the general solution to the differential equation. By imposing the temperature boundary condition at each end of the element, a finite element interpolation function can be formulated in terms of the meridional coordinate, the end temperatures T_1 and T_2, and a nodeless parameter T_0. An element's temperature interpolation function is written as[2]

$$T(s)=N_0(s)T_0+N_1(s)T_1+N_2(s)T_2 \tag{3}$$

Element interpolation functions derived in the form of Eq. (3) are not generally the same as used in conventional finite elements since they result from the differential-equation solution. These functions may be simple polynomials or transcendental functions depending on the solution of Eq. (2). Exact expressions for the temperature interpolation functions used in this Note are tabulated in Ref. 2.

For the structural analysis, a geometrically exact shell element with seven degrees of freedom per nodal circle is employed. The interpolation functions for this element are expressed as a Fourier series in the circumferential direction

Presented as Paper 82-0701 at the AIAA/ASME/ASCE/AHS 23rd Structures, Structural Dynamics and Materials Conference, New Orleans, La., May 10-12, 1982; submitted May 12, 1982; revision received Dec. 7, 1982.

*Assistant Professor, Civil Engineering Department.
†Professor, Mechanical Engineering and Mechanics Department.